

# *Ab initio* modeling of resonant inelastic x-ray scattering from $\text{Ca}_2\text{RuO}_4$

D. A. Kukusta,<sup>1</sup> L. V. Bekenov,<sup>1</sup> P. F. Perndorfer,<sup>2,3</sup> D. V. Vyalikh,<sup>4,5</sup> P. A. Buczek,<sup>3</sup> A. Ernst,<sup>2,6</sup> and V. N. Antonov<sup>1,7</sup>

<sup>1</sup>*G. V. Kurdyumov Institute for Metal Physics of the N.A.S. of Ukraine, 36 Academician Vernadsky Boulevard, UA-03142 Kyiv, Ukraine*

<sup>2</sup>*Institute for Theoretical Physics, Johannes Kepler University, Altenberger Strasse 69, A-4040 Linz, Austria*

<sup>3</sup>*Department of Engineering and Computer Sciences,*

*Hamburg University of Applied Sciences, Berliner Tor 7, D-20099 Hamburg, Germany*

<sup>4</sup>*Donostia International Physics Center (DIPC), 20018 Donostia-San Sebastián, Spain*

<sup>5</sup>*IKERBASQUE, Basque Foundation for Science, 48011 Bilbao, Spain*

<sup>6</sup>*Max Planck Institute of Microstructure Physics, D-06120 Halle (Saale), Germany*

<sup>7</sup>*Max-Planck-Institute for Solid State Research, Heisenbergstrasse 1, 70569 Stuttgart, Germany*

(Dated: November 26, 2025)

The single-layered perovskite  $\text{Ca}_2\text{RuO}_4$ , characterized by a  $4d^4$  electron configuration, has been studied from first principles using density functional theory (DFT) using the generalized gradient approximation, with inclusion of strong on-site Coulomb interactions and spin-orbit coupling (GGA+SO+ $U$ ), in the framework of the fully relativistic, spin-polarized Dirac linear muffin-tin orbital (LMTO) band-structure method. This approach enabled a comprehensive investigation of the electronic structure of  $\text{Ca}_2\text{RuO}_4$  through the modeling of relevant spectra obtained from synchrotron-based techniques widely used to probe electronic properties, with a primary focus on resonant inelastic X-ray scattering (RIXS) at the Ru  $L_3$  and O  $K$  edges. The calculated spectra were thoroughly analyzed with available experimental data reported in the literature. The good agreement between our results and experimental observations for  $\text{Ca}_2\text{RuO}_4$  enables a conclusive interpretation of key features in the spectra obtained from the aforementioned techniques. Consequently, this enables us to describe its electronic properties and to establish a solid theoretical approach suitable for routine modeling of spectra, particularly from RIXS, aimed at characterizing the electronic structure and properties of similar or more complex strongly correlated, technologically relevant materials.

PACS numbers: 75.50.Cc, 71.20.Lp, 71.15.Rf

## I. INTRODUCTION

Due to the extended nature of  $4d$  and  $5d$  wave functions and the resulting broad energy bands in solids,  $4d$  and  $5d$  transition-metal oxides are naturally expected to behave as weakly correlated materials. However, driven by strong spin-orbit coupling (SOC), many of these compounds exhibit a Mott-insulating state and, as a consequence, display unusual electronic and magnetic properties [1, 2]. The strong SOC in  $d$  systems split the  $t_{2g}$  orbitals into a Kramers quartet ( $J_{\text{eff}} = 3/2$ ) and a doublet ( $J_{\text{eff}} = 1/2$ ) [3–5]. When, in addition to strong SOC, electron correlations emerge, this can give rise to such fascinating phenomena as Mott insulators [1–3, 10, 11], topological insulators [6–9], Weyl semimetals [12–14], and quantum spin liquids [3, 15]. So far, most research efforts have focused on  $d^{4+}$  systems with a  $t_{2g}^5$  configuration [1, 16–19]. For such materials, for example, the layered perovskite  $\text{Sr}_2\text{IrO}_4$ , the quartet  $J_{\text{eff}} = 3/2$  is fully occupied, and the relatively narrow  $J_{\text{eff}} = 1/2$  doublet occupied by one electron can be already split by moderate Hubbard  $U_{\text{eff}}$  with opening a small band gap called the relativistic Mott gap [1, 11, 20].

Another broad family of magnetic Mott-insulating  $d$ -electron systems, which often exhibit peculiar electronic and magnetic properties, is that with a completely empty Kramers upper  $J_{\text{eff}} = 1/2$  doublet and a partially filled

lower  $J_{\text{eff}} = 3/2$  quartet of the  $t_{2g}$  orbitals. There are several possibilities with partially filled  $t_{2g}$  orbitals, namely,  $d^1$ ,  $d^2$ ,  $d^3$ , and  $d^4$  cases. Mott insulators with  $d^1$  and  $d^2$  configurations have been shown to exhibit exotic magnetic phases [21–24] in the presence of large SOC. In the  $d^3$  case, SOC is quenched in a cubic environment [23]. For a  $d^4$  electron configuration ( $t_{2g}^4 e_g^0$ ) the system is expected to be nonmagnetic in both the weakly and strongly correlated limits. In the weakly correlated picture, when the SOC dominates over the Hund's coupling,  $t_{2g}$  shells are split into a fully filled  $J_{\text{eff}} = 3/2$  shell and an empty  $J_{\text{eff}} = 1/2$  shell due to strong SOC. SOC then opens up a band gap between the  $J_{\text{eff}} = 3/2$  and  $J_{\text{eff}} = 1/2$  bands leading to a nonmagnetic insulating ground state. In the strongly correlated picture, the first two Hund's rules require each  $d^4$  site to have total  $S = 1$  and  $L = 1$ . The SOC then yields a local  $J = 0$  state on every ion with a nonmagnetic ground state [22, 25].

Although octahedrally coordinated  $\text{Re}^{3+}$ ,  $\text{Os}^{4+}$ ,  $\text{Ir}^{5+}$ , and  $\text{Ru}^{4+}$  systems with a  $d^4$  electronic configuration have been known since the 1960s [26], they have been largely overlooked over the years. However, following the report of long-range magnetic order in  $\text{Sr}_2\text{YIrO}_6$  [27] and the proposal of a condensation mechanism for magnetism in  $d^4$  Mott insulators [28],  $d^4$  electron systems have recently attracted significant interest.

We consider here the electronic structure and physi-

cal properties of the single-layered perovskite  $\text{Ca}_2\text{RuO}_4$  which belongs to the so-called Ruddlesden-Popper (RP) type ruthenates  $\text{A}_{n+1}\text{Ru}_n\text{O}_{3n+1}$  ( $\text{A} = \text{Sr}$  or  $\text{Ca}$ ), where  $n$  is the number of Ru-O layers per unit cell. These ruthenates have recently received significant attention due to the discovery of their fascinating physical properties. For example,  $\text{Sr}_2\text{RuO}_4$  ( $n = 1$ ) exhibits unconventional  $p$ -wave superconductivity [29, 30], whereas  $\text{Ca}_2\text{RuO}_4$  is a typical Mott insulator [31]. In the  $n = \infty$  family  $\text{SrRuO}_3$  is a ferromagnetic metal [31], whereas  $\text{CaRuO}_3$  does not show any magnetic ordering [32].

The  $\text{Ca}_2\text{RuO}_4$  discussed here is a topical material exhibiting a wealth of physical properties. Among them, a record-high nonsuperconducting diamagnetic response has been reported [33]. Superconductivity emerges in strained films [34] or upon application of hydrostatic pressure to bulk crystals [35]. Next,  $\text{Ca}_2\text{RuO}_4$  is reported to undergo a series of phase transitions upon cooling: a metal-to-insulator transition at 357 K [36–39], orbital ordering at 260 K [40, 41], and antiferromagnetic (AFM) ordering at 110 K [36, 37, 40, 41]. Neutron and Raman scattering experiments have demonstrated the existence of a spin-orbit exciton [42–45]. Because it remains insulating above the Néel temperature and exhibits Curie-Weiss magnetic susceptibility,  $\text{Ca}_2\text{RuO}_4$  [46] is widely recognized as a Mott insulator. The momentum-resolved photoemission (ARPES) measurements of the paramagnetic insulating band structure [47] have also been interpreted in favor of an orbitally differentiated band-Mott insulating ground state [48]. This rich phenomenology of  $\text{Ca}_2\text{RuO}_4$  reflects the intricate interplay between the Coulomb interaction  $U$ , Hund’s coupling  $J_H$ , crystal electric field (CEF) splitting, and SOC.

The essential part of our work is dedicated to a comprehensive *ab-initio* theoretical characterization of the electronic structure of  $\text{Ca}_2\text{RuO}_4$ , with a focus on modeling of Resonant Inelastic X-ray Scattering (RIXS) spectra at the Ru  $L_3$  and O  $K$  edges of this material, along with their analysis, interpretation, and comparison with existing literature data. Since the first publication by Kao *et al.* on NiO [49], the RIXS method has shown remarkable progress as a spectroscopic technique to record the momentum and energy dependence of inelastically scattered photons in complex materials. RIXS rapidly became the forefront of experimental photon science [50, 51]. It combines spectroscopy and inelastic scattering to probe the electronic structure of materials. This method is an element- and orbital- selective X-ray spectroscopy technique, based on a two-step, two-photon resonant process. It combines X-ray emission spectroscopy (XES) with X-ray absorption spectroscopy (XAS) by measuring the coherent X-ray emission at an incident X-ray photon energy within the near edge X-ray absorption spectrum. In the first step (X-ray absorption), an electron of the absorbing atom is resonantly excited from a core level to an empty state. The resulting state, called the intermediate state, carries a core hole with a very small lifetime. In the second step (X-ray emission), the system radiatively

decays into a final state in which the core hole is filled by another electron accompanied by photon-out emission. The polarization of the incoming and outgoing light and the resonant energy are involved in the RIXS process, making RIXS a simultaneous spectroscopy and scattering technique. RIXS has a number of unique features in comparison with other spectroscopic techniques. It covers a large scattering phase space and requires only small sample volumes. Because RIXS is a photon-in, photon-out technique, it is truly bulk sensitive, with negligible contributions from surface effects. Additionally, RIXS is polarization dependent, and both element- and orbital-specific [50]. A detailed comparison with other spectroscopic techniques can be found in a recent review [51]. Spectral broadening due to the short core-hole lifetime can be minimized, to produce RIXS spectra with high energy and momentum resolution. This enables direct probing of quasiparticles and their properties, such as phonons, plasmons, single magnons, and orbitons, their mutual interplay, as well as other many-body excitations in strongly correlated systems, including cuprates, nickelates, osmates, ruthenates, and iridates, which exhibit complex and exotic low-energy physics manifested by fine structure of excitations in energy-momentum space.

Significant progress in RIXS experiments has been achieved over the past decade. However, most theoretical modeling of RIXS spectra has relied on the atomic multiplet approach with empirical parameter adjustments. First-principles calculations of RIXS spectra remain exceedingly rare. Thus, the most essential point of our paper is to introduce an *ab initio* theoretical approach for modeling RIXS spectra and to demonstrate its application to the highly nontrivial and complex material  $\text{Ca}_2\text{RuO}_4$ .

Extensive experimental RIXS investigations of  $\text{Ca}_2\text{RuO}_4$  have been reported, with the key findings summarized below. We begin with the work of Grestarsson *et al.* [45], who measured and characterized the RIXS spectra at the Ru  $L_3$  edge. They have uncovered a series of sharp electronic excitations at low energy in  $\text{Ca}_2\text{RuO}_4$  at  $\sim 0.05$ , 0.32, 0.75, and 1.0 eV. They found strong photon polarization dependence of the RIXS intensity at 0.32 eV with varying the incident angle  $\theta$  from  $9^\circ$  to  $77^\circ$ . The authors have carried out ionic model calculations that quantify the energy levels of Ru  $d^4$  multiplets and corresponding RIXS intensities. The ionic model Hamiltonian which includes the intraionic Coulomb interactions, SOC, and CEF was used. The lowest peak was interpreted as magnetic excitations in consistency with neutron and Raman scattering measurements [43, 44]. The authors interpreted the excitation at 0.32 eV as a SOC-driven  $J = 0 \rightarrow 2$  transition. The peaks at 0.75 and 1.0 eV were found to be due to Hund’s-rule driven  $S = 1 \rightarrow 0$  spin-state transitions, split by the tetragonal CEF. The multiplets at higher energies (2-4 eV) correspond to excitations from the  $t_{2g}$  ground-state manifold of the Ru ions into the  $e_g$  CEF levels. Kim *et al.* [52] present a similar classification of

the Ru  $L_3$  RIXS spectrum by developing a comprehensive theory description of the RIXS spectrum using the general RIXS operators introduced in Ref. [53]. Analytic solutions were provided for the collective magnetic excitations and for their RIXS transitions in terms of the pseudospin operators. The authors found that the  $J = 2$  transitions at 0.32 eV show huge spectral weights and exhibit prominent polarization dependence in agreement with the experimental observation [45]. Bertinshaw *et al.* [54] present the RIXS Ru  $L_3$  spectrum in  $\text{Ca}_2\text{RuO}_4$  in a wide energy interval up to 6.2 eV and compare it with the corresponding spectrum in the structurally related Mott insulator  $\text{Ca}_3\text{Ru}_2\text{O}_7$ .

Yamamoto *et al.* [55] investigated the low-energy excitation ( $\leq 1.5$  eV) RIXS spectra in  $\text{Ca}_2\text{RuO}_4$  using the three-orbital Hubbard model obtained by the band-structure calculation and applying random-phase approximation (RPA). The energy band structure of  $\text{Ca}_2\text{RuO}_4$  calculated by the mean-field approximation with  $U_{\text{eff}} = 1.53$  eV. By the fast-collision approximation, they calculated the Ru  $L_3$  RIXS spectra from the dynamical susceptibilities. The authors show that the dispersion of the transverse mode is clearly observed in the calculated RIXS spectra and that the polarization dependence of the incident X-rays enables one to distinguish between the excitations of the in-plane and out-of-plane transverse modes.

In this study, we present a comprehensive *ab initio* DFT analysis of the electronic structure and RIXS spectra of  $\text{Ca}_2\text{RuO}_4$  over an extended energy range. We calculated the band structure and modeled the RIXS spectra using the fully relativistic, spin-polarized Dirac linear muffin-tin orbital (LMTO) method. To assess the impact of electron correlation, we employed the generalized gradient approximation (GGA) together with the GGA+ $U$  approach. Overall, our work provides key insights into the influence of transition-metal  $4d$ -O  $2p$  hybridization and properties of the band-structure on RIXS spectra not only of  $\text{Ca}_2\text{RuO}_4$  but of  $4d$  oxides in general.

The paper is organized as follows. Section II describes the crystal structure of  $\text{Ca}_2\text{RuO}_4$  and the computational methodology. Section III presents the results of the electronic structure of  $\text{Ca}_2\text{RuO}_4$ . Section IV discusses the theoretical investigations of XES, XAS, and XMCD spectra. Section V presents the *ab initio* RIXS spectra at the Ru  $L_3$  and O  $K$  edges, and compares them with experimental data. Finally, Section VI summarizes our conclusions.

## II. DETAILS OF THEORETICAL METHODOLOGY

### A. Modeling of RIXS spectra

RIXS refers to the process where the material first absorbs a photon. The system then is excited to a short-lived intermediate state, from which it relaxes radiatively.

In an experiment, one studies the X-rays emitted in this decay process. In the direct RIXS process [50] an incoming photon with energy  $\hbar\omega_{\mathbf{k}}$ , momentum  $\hbar\mathbf{k}$  and polarization  $\boldsymbol{\epsilon}$  excites the solid from a ground state  $|g\rangle$  with energy  $E_g$  to the intermediate state  $|I\rangle$  with energy  $E_I$ . During relaxation the outgoing photon with energy  $\hbar\omega_{\mathbf{k}'}$ , momentum  $\hbar\mathbf{k}'$  and polarization  $\boldsymbol{\epsilon}'$  is emitted, and the solid is in the state  $|f\rangle$  with energy  $E_f$ . A valence electron is excited from state  $\mathbf{k}$  to states  $\mathbf{k}'$  with energy  $\hbar\omega = \hbar\omega_{\mathbf{k}} - \hbar\omega_{\mathbf{k}'}$  and momentum transfer  $\hbar\mathbf{q} = \hbar\mathbf{k} - \hbar\mathbf{k}'$ . The RIXS intensity can in general be presented in terms of a scattering amplitude as [50]

$$I(\omega, \mathbf{k}, \mathbf{k}', \boldsymbol{\epsilon}, \boldsymbol{\epsilon}') = \sum_f |T_{fg}(\mathbf{k}, \mathbf{k}', \boldsymbol{\epsilon}, \boldsymbol{\epsilon}', \omega_{\mathbf{k}})|^2 \times \delta(E_f + \hbar\omega_{\mathbf{k}'} - E_g - \hbar\omega_{\mathbf{k}}), \quad (1)$$

where the delta function enforces energy conservation and the amplitude  $T_{fg}(\mathbf{k}, \mathbf{k}', \boldsymbol{\epsilon}, \boldsymbol{\epsilon}', \omega_{\mathbf{k}})$  reflects which excitations are probed and how, for instance, the spectral weights of final state excitations depend on the polarization vectors  $\boldsymbol{\epsilon}$  and  $\boldsymbol{\epsilon}'$  of the incoming and outgoing x-rays, respectively.

Our implementation of the code for the calculation of the RIXS intensity uses Dirac four-component basis functions [56] in the perturbative approach [57]. RIXS is a second-order process, and its intensity is given by

$$I(\omega, \mathbf{k}, \mathbf{k}', \boldsymbol{\epsilon}, \boldsymbol{\epsilon}') \propto \sum_f \left| \sum_I \frac{\langle f | \hat{H}'_{\mathbf{k}'\boldsymbol{\epsilon}'} | I \rangle \langle I | \hat{H}'_{\mathbf{k}\boldsymbol{\epsilon}} | g \rangle}{E_g - E_I} \right|^2 \times \delta(E_f - E_g - \hbar\omega), \quad (2)$$

where the delta function enforces energy conservation, and the photon absorption operator in the dipole approximation is given by the lattice sum  $\hat{H}'_{\mathbf{k}\boldsymbol{\epsilon}} = \sum_{\mathbf{R}} \hat{\boldsymbol{\alpha}}\boldsymbol{\epsilon} \exp(-i\mathbf{k}\mathbf{R})$ , where  $\hat{\boldsymbol{\alpha}}$  are Dirac matrices. Both  $|g\rangle$  and  $|f\rangle$  states are dispersive so the sum over final states is calculated using the linear tetrahedron method [58]. The matrix elements of the RIXS process in the frame of the fully relativistic Dirac LMTO method were presented in our previous publication [59].

### B. Crystal structure

$\text{Ca}_2\text{RuO}_4$  is reported to undergo a series of phase transitions upon cooling; a metal-to-insulator transition at 357 K [36–39], an orbital ordering at 260 K [40, 41], and an AFM ordering at 110 K [36, 37, 40, 41]. At low temperature below 180 K  $\text{Ca}_2\text{RuO}_4$  is crystallized in the simple orthorhombic structure (space group  $Pbca$ , No. 61) which is characterized by a rotation of the octahedra around the  $c$  axis with a tilt around an axis parallel to an edge of the octahedron basal plane [38].

The lattice parameters of  $\text{Ca}_2\text{RuO}_4$  are given in Table I. The  $\text{RuO}_6$  octahedra are tilted and rotated, as

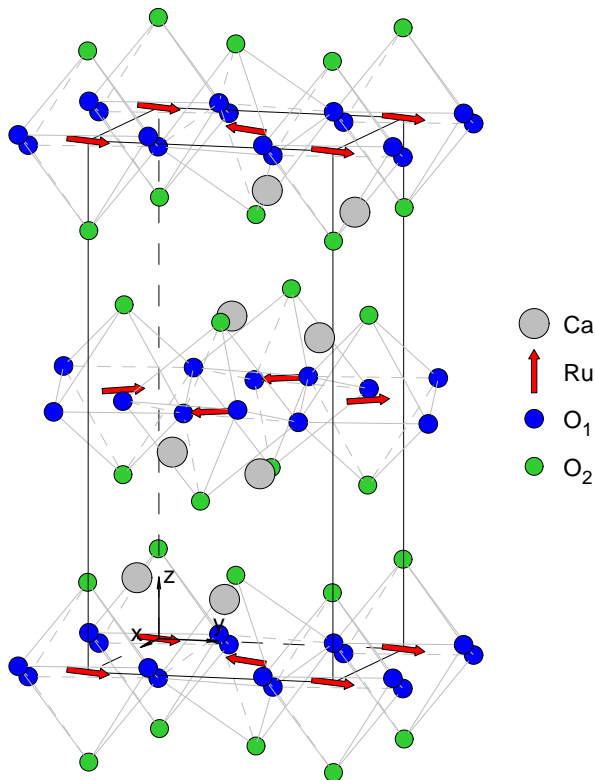


FIG. 1: (Color online) Schematic representation of the AFM structure of Ru ions (red arrows) in  $\text{Ca}_2\text{RuO}_4$  (space group  $Pbca$ , number 61). Grey spheres represent Ca atoms, blue and green spheres show oxygen atoms.

TABLE I: Atomic positions in  $\text{Ca}_2\text{RuO}_4$  ( $Pbca$ ). The lattice parameters for  $\text{Ca}_2\text{RuO}_4$  are equal to  $a = 5.3945 \text{ \AA}$ ,  $b = 5.5999 \text{ \AA}$ ,  $c = 11.7653 \text{ \AA}$  [38].

Atom	WC	$x$	$y$	$z$
Ca	$8c$	0.0042	0.0559	0.3524
Ru	$4a$	0	0	0
O <sub>1</sub>	$8c$	0.1961	0.3018	0.0264
O <sub>2</sub>	$8c$	-0.0673	-0.0218	0.1645

seen in Fig. 1. Each  $\text{RuO}_6$  octahedron is flattened since the bond distance between Ru and apical oxygen  $\text{Ru-O}_2$  ( $= 1.9729 \text{ \AA}$ ) is shorter than the in-plane  $\text{Ru-O}_1$  bond distances ( $= 2.0040 \text{ \AA}$ ).

### C. Details of Computations

The details of the computational method are described in our previous papers [59–62] and here we only mention several aspects. The band structure calculations were performed using the fully relativistic linear muffin-tin orbital (LMTO) method [63, 64]. This implementation of the LMTO method uses four-component basis func-

tions constructed by solving the Dirac equation inside an atomic sphere [56]. The exchange-correlation functional of the generalized gradient approximation (GGA)-type was used in the version of Perdew, Burke and Ernzerhof [65]. The Brillouin zone (BZ) integration was performed using the improved tetrahedron method [66]. The basis consisted of Ru and Ca  $s$ ,  $p$ ,  $d$ , and  $f$ ; and O  $s$ ,  $p$ , and  $d$  LMTO's.

To take into account the electron-electron correlation effects, we used in this work the relativistic generalization of the rotationally invariant version of the LSDA+ $U$  method [67] which takes into account that in the presence of SOC the occupation matrix of localized electrons becomes non-diagonal in spin indexes. Hubbard  $U$  was considered as an external parameter and varied from 0.7 eV to 3.7 eV. We used in our calculations the value of exchange Hund's coupling  $J_H=0.7 \text{ eV}$  obtained from constrained LSDA calculations [68, 69]. Thus, the parameter  $U_{\text{eff}} = U - J_H$ , which roughly determines the splitting between the lower and upper Hubbard bands, varied between 0 eV and 3.0 eV. We adjusted the value of  $U$  to achieve the best agreement with the experiment.

In the RIXS process, an electron is promoted from a core level to an intermediate state, leaving behind a core hole. As a result, the electronic structure of that intermediate state differs from that of the ground state. In order to reproduce the experimental spectrum the self-consistent calculations should be carried out including a core hole. Usually, the core-hole effect has no impact on the shape of XAS spectra at the  $L_{2,3}$  edges of the  $5d$  systems and just a minor impact on the XMCD spectra at these edges [64]. However, the core hole has a strong impact on the RIXS spectra in transition metal compounds [59, 70], therefore, we take it into account.

The XAS, XMCD, and RIXS spectra were calculated taking into account the exchange splitting of core levels. The finite lifetime of a core hole was accounted for by folding the spectra with a Lorentzian. The widths of core levels for Ru and O were taken from Ref. [71]. The finite experimental resolution of the spectrometer was accounted for by a Gaussian of 0.6 eV (the  $s$  coefficient of the Gaussian function).

Note that in our electronic structure calculations, we rely on experimentally measured atomic positions and lattice parameters [38] (see Table I) because they are well established for these materials and are probably still more accurate than those obtained from DFT.

## III. ELECTRONIC STRUCTURE

In order to gain insight about the ground state magnetic configurations of  $\text{Ca}_2\text{RuO}_4$  we compared the calculated total energies for different spin ordering in  $\text{Ca}_2\text{RuO}_4$ , namely, nonmagnetic (NM), ferromagnetic (FM), and AFM. For AFM phases we consider three types of ordering along the  $c$  ( $\text{AFM}_{001}$ ),  $a$  ( $\text{AFM}_{100}$ ), and  $b$  ( $\text{AFM}_{010}$ ) axes. We also consider possible non-

TABLE II: The total energy  $E_{total}$  per formula unit (in meV) calculated in the GGA approximation for the nonmagnetic configuration, and in the GGA+SO approximation for the nonmagnetic configuration, ferromagnetic ordering along the (001) axis ( $FM_{001}$ ), antiferromagnetic (AFM) ordering along the (001) axis ( $AFM_{001}$ ), AFM ordering along the (100) axis ( $AFM_{100}$ ), AFM ordering along the (010) axis ( $AFM_{010}$ ), and canted noncollinear AFM ordering almost along the (010) axis ( $AFM_{010}^{NC}$ ) defined relative to  $AFM_{010}^{NC}$ .

GGA	GGA+SO	$FM_{001}$	$AFM_{001}$	$AFM_{100}$	$AFM_{010}$	$AFM_{010}^{NC}$
12.647	3.383	7.652	1.120	0.329	0.098	0.0

collinear (NC) magnetic structures. Our GGA+SO band structure calculations show that the canted NC configuration shown in Fig. 1 with Ru spins ordered antiferromagnetically almost along the (010) direction ( $AFM_{010}^{NC}$ ) possesses the lowest total energy in comparison with the NM, FM, AFM ordering along the  $a$ ,  $b$ , and  $c$  directions (Table II). The NC polar angles equal to  $\theta_{Ru}=95.4^\circ$  and  $\phi_{Ru}=\pm 95.8^\circ$ . Similar results are obtained also in the GGA+SO+ $U$  approximation, the results are found to be robust against changes in the parameter  $U_{eff}$ . This is consistent with the conclusion made by Porter *et al.* [41] regarding AFM canting in  $Ca_2RuO_4$ , based on detailed resonant elastic x-ray scattering (REXS) measurements at the Ru  $L_{2,3}$  edges. Their results indicate that the magnetic moment is not strictly confined to the  $b$  axis, as previously suggested, but instead has a component along the  $c$  axis amounting to approximately one tenth of the total moment [41].

Figure 2 establishes a picture of the SOC-driven Mott transition in  $Ca_2RuO_4$ . In the absence of SOC, the partially filled bands of predominantly  $t_{2g}$  orbital character would lead to a metallic ground state [Fig. 2(a,b,c)]. The GGA approach for the FM ordering produces a half-metallic solution with the energy gap for spin up states. The Fermi energy is located near a local minimum in the DOS for the AFM solution [Fig. 2(c)].

The fully relativistic GGA+SO bands are presented in Fig. 2(d) by circles proportional in size to their orbital character projected onto the basis set of Ru  $d_{3/2}$  (the relativistic quantum number  $\kappa = 2$ , the blue curve) and  $d_{5/2}$  ( $\kappa = -3$ , the red curve) states. In  $Ca_2RuO_4$  each  $Ru^{4+}$  ion surrounded by six  $O^{2-}$  ions has four valent  $4d$  electrons. The octahedral crystal field largely splits the Ru  $t_{2g}$  and  $e_g$  manifolds, so that all four electrons occupy the  $t_{2g}$  manifold. As a result of strong SOC, the six  $t_{2g}$  orbitals are further separated into two manifolds with  $J_{eff} = 3/2$  and  $J_{eff} = 1/2$ . The  $J_{eff} = 3/2$  states are fully filled and  $J_{eff} = 1/2$  states are empty, which is consistent with our expectations. The functions of the  $J_{eff} = 3/2$  quartet are dominated by  $d_{3/2}$  states with some minor weight of  $d_{5/2}$  ones, which is determined by the relative strengths of SOC and crystal-field splitting. The  $J_{eff} = 1/2$  functions, on the other hand, are given by

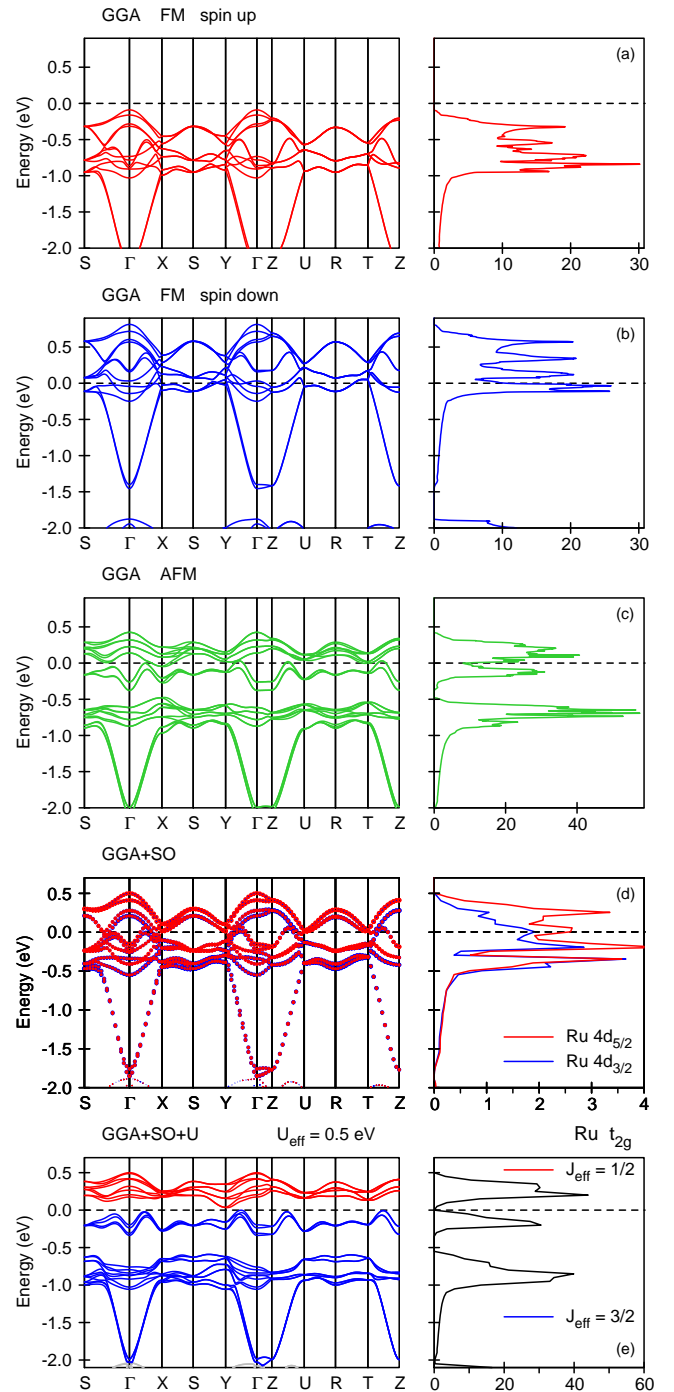


FIG. 2: (Color online) The  $t_{2g}$  energy band structure of  $Ca_2RuO_4$  calculated in the GGA approach without SOC for the FM ordering for the spin up (a) and spin down (b) states. The panel (c) shows the energy bands for the AFM ordering in the GGA approach. The panel (d) presents the fully relativistic Dirac GGA+SO approximation. The bands crossing the Fermi level which have almost pure  $d_{5/2}$  character (open red circles) are formed by  $t_{2g}$  states with  $J_{eff} = 1/2$ . The lower panel (e) presents the  $t_{2g}$  energy bands calculated in the GGA+SO+ $U$  approximation with  $U_{eff} = 0.5$  eV for the canted noncollinear AFM ordering  $AFM_{010}^{NC}$ .

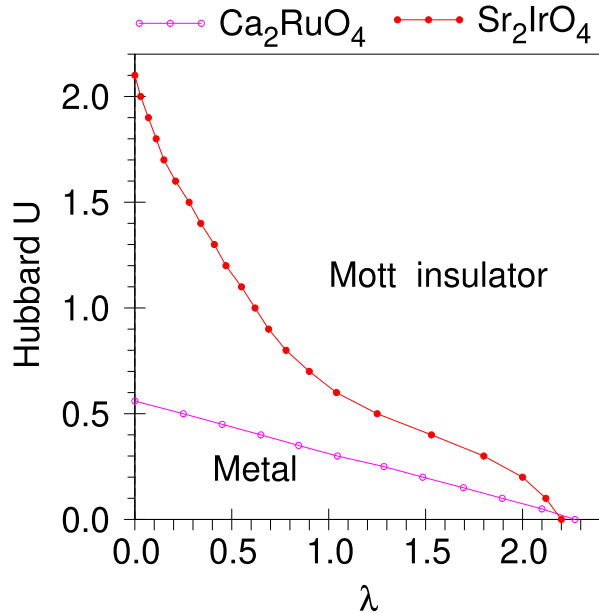


FIG. 3: (Color online) The phase diagram in the  $U_{\text{eff}}-\text{SOC}$  plane for  $\text{Ca}_2\text{RuO}_4$  in comparison with  $\text{Sr}_2\text{IrO}_4$  [72]. The solid-circled lines separates metal and Mott insulator states connected via a first-order phase transition.

linear combinations of  $d_{5/2}$  states only [Fig. 2(d)]. This allows one to identify bands with pure  $d_{5/2}$  character as originating from  $J_{\text{eff}} = 1/2$  states.

The lower panel (e) of Fig. 2 presents the  $t_{2g}$  energy bands calculated in the GGA+SO+ $U$  approximation with  $U_{\text{eff}} = 0.5$  eV for the canted noncollinear AFM ordering ( $\text{AFM}_{010}^{\text{NC}}$ ) with the energy gap between fully occupied  $J_{\text{eff}} = 3/2$  and empty  $J_{\text{eff}} = 1/2$  states.

It is useful to compare  $\text{Ca}_2\text{RuO}_4$  with  $\text{Sr}_2\text{IrO}_4$ , as the latter is less correlated due to its  $5d$  electrons, compared to the  $4d$  electrons in  $\text{Ca}_2\text{RuO}_4$ . Because of this,  $\text{Sr}_2\text{IrO}_4$  would be expected to show a weaker tendency toward magnetism. On the other hand,  $\text{Sr}_2\text{IrO}_4$  has only a single hole in the  $t_{2g}$  manifold, as opposed to two in  $\text{Ca}_2\text{RuO}_4$  ( $5d^5$  versus  $4d^4$  electrons, respectively), and stronger spin-orbit interaction. In  $\text{Sr}_2\text{IrO}_4$  for the nonmagnetic solution the energy gap does not open up for any, even very large, Hubbard parameter  $U$  [72]. In the case of  $\text{Ca}_2\text{RuO}_4$  for the nonmagnetic solution the insulating gap opens up at the critical value for the  $U_{\text{eff}}^c = 2.05$  and  $1.4$  eV in the GGA (without SOC) and GGA+SO (with SOC) approximations, respectively. For the FM ordering the gap opens up at  $U_{\text{eff}}^c = 1.2$  eV for the GGA+SO approach. For the collinear AFM ordering the gap opens up at smaller  $U_{\text{eff}}^c = 1.0$  eV. For the ground state noncollinear canted  $\text{AFM}_{010}^{\text{NC}}$  ordering the gap opens up for even smaller  $U_{\text{eff}}^c = 0.35$  eV. We can conclude that magnetic ordering plays an important role in the gap formation in  $\text{Ca}_2\text{RuO}_4$ , therefore, this oxide has a mixed Slater and Mott character.

Figure 3 presents a phase diagram in the  $U_{\text{eff}}-\text{SOC}$

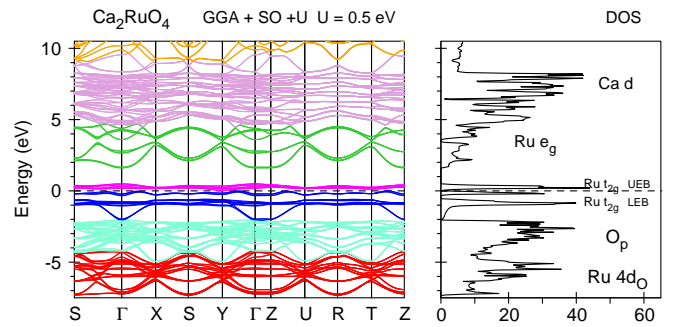


FIG. 4: (Color online) The *ab initio* energy band structure of  $\text{Ca}_2\text{RuO}_4$  calculated in the GGA+SO+ $U$  with  $U_{\text{eff}} = 0.5$  eV approximation.

plane for  $\text{Ca}_2\text{RuO}_4$  in comparison with  $\text{Sr}_2\text{IrO}_4$  [72]. To obtain this diagram, we tune the SOC term for the Ru  $4d$  orbitals. A scaling factor  $\lambda$  in the SOC term of the Hamiltonian is introduced in the second variational step [73]. In this way, we can enhance the effect of SOC by taking  $\lambda > 1$  or reduce it by taking  $\lambda < 1$ . For  $\lambda = 0$  there is no SOC at all, while  $\lambda = 1$  refers to the self-consistent reference value. The open-circled magenta line in Fig. 3 separates metal and Mott insulator states for  $\text{Ca}_2\text{RuO}_4$ , which are connected via a first-order phase transition, calculated in the GGA+SO+ $U$  approximation for the canted  $\text{AFM}_{010}^{\text{NC}}$  order. For  $\lambda = 0$  the energy gap opens up for  $U_{\text{eff}}^c = 0.56$  eV and  $U_{\text{eff}}^c = 0$  eV for  $\lambda = 2.27$ . The greater the value of  $U_{\text{eff}}$ , the lower the value of  $\lambda$  is for the phase transition.

In the case of  $\text{Sr}_2\text{IrO}_4$ , for  $\lambda = 0$  the energy gap opens up for  $U_{\text{eff}}^c = 2.1$  eV and  $U_{\text{eff}}^c = 0$  eV for  $\lambda = 2.2$  (the solid-circled red line in Fig. 3) [72]. We can conclude that  $\text{Ca}_2\text{RuO}_4$  is a more strong Mott dielectric than  $\text{Sr}_2\text{IrO}_4$  because it possesses much larger  $U_{\text{eff}}-\text{SOC}$  phase space in comparison with  $\text{Sr}_2\text{IrO}_4$ .

Figures 4 and 5 present the *ab initio* energy band structure and partial DOSs of  $\text{Ca}_2\text{RuO}_4$  for the noncollinear canted  $\text{AFM}_{010}^{\text{NC}}$  ordering, calculated in the fully relativistic Dirac approximation with taking into account Coulomb correlations in the GGA+SO+ $U$  approximation for  $U_{\text{eff}} = 0.5$  eV. This value of Hubbard  $U$  produces the best agreement between the theoretically calculated and experimentally measured RIXS spectra at the Ru  $L_3$  and oxygen  $K$  edges (see Section V).

Four electrons occupy the  $t_{2g}$ -type low energy band (LEB) manifold which consists of two separate peaks situated in the energy intervals from  $-2.0$  to  $-0.55$  eV and from  $-0.34$  eV to  $E_F$ . The empty  $t_{2g}$  states [the upper energy band (UEB)] have one DOS peak and occupy the energy range from  $0.04$  eV to  $0.5$  eV (see Fig. 5). The  $e_g$ -type states of Ru are distributed far above the Fermi level from  $1.6$  eV to  $4.6$  eV. The  $3d$  states of Ca ions are mostly situated above the Fermi level from  $4.6$  to  $9.1$  eV. The occupation number of  $4d$  electrons in the Ru atomic sphere in  $\text{Ca}_2\text{RuO}_4$  is equal to  $5.77$ , which is much larger

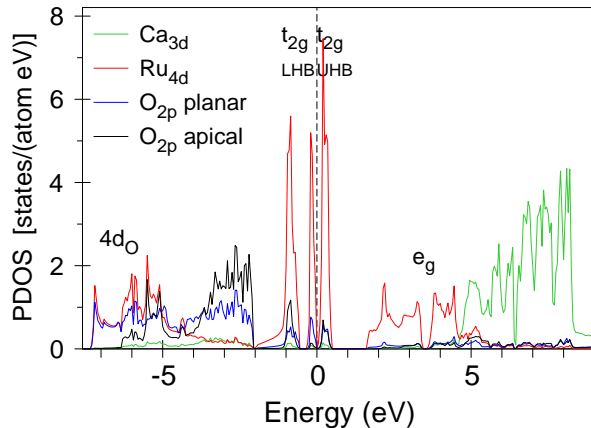


FIG. 5: (Color online) The partial density of states DOS [in states/(atom eV)] in  $\text{Ca}_2\text{RuO}_4$  calculated in the GGA+SO+ $U$  approximation ( $U_{\text{eff}} = 0.5$  eV).

than the expected value of four  $t_{2g}$  electrons. The excessive charge is provided by the tails of oxygen 2p states. These  $4d_{\text{O}}$  states are located at the bottom of oxygen 2p states from  $-7.3$  eV to  $-4.1$  eV and play an essential role in the RIXS spectrum at the Ru  $L_3$  edge (see Section V).

The electronic structures of apical  $\text{O}_2$  and in-plane  $\text{O}_1$  ions significantly differ from each other. The apical  $\text{O}_2$  2s states consist of four very narrow peaks situated at  $-17.5$  and  $-16.7$  eV. The in-plane  $\text{O}_1$  2s states possess a relatively wider two peak structure from  $-18.9$  to  $-17.7$  eV (not shown). The oxygen 2p states are situated just below Ru LEB between  $-2.1$  and  $-7.3$  eV. The in-plane  $\text{O}_1$  2p states hybridize with Ru 4d states in the energy interval from  $-7.3$  to  $-4.1$  eV, while the apical  $\text{O}_2$  2p states hybridize with Ru 4d states in the smaller energy interval from  $-6.4$  to  $-4.1$  eV. The small peaks in the close vicinity of the Fermi level from  $-2.0$  to  $E_F$  and from  $0.04$  eV to  $0.5$  eV are due to the strong hybridization between O 2p and Ru  $t_{2g}$  LEB and UEB, respectively.

The theoretically calculated spin  $M_s$ , orbital  $M_l$ , and total  $M_{\text{total}}$  magnetic moments using the GGA+SO+ $U$  approach ( $U_{\text{eff}} = 0.5$  eV) for the canted AFM $_{010}^{\text{NC}}$  solution are equal to  $1.2718 \mu_B$ ,  $0.2643 \mu_B$ , and  $1.5361 \mu_B$ , respectively. The spin and orbital magnetic moments at the Ca site are relatively small ( $M_s = 0.0054 \mu_B$  and  $M_l = 0.0008 \mu_B$ ). The magnetic moments for in-plane  $\text{O}_1$  ions are equal to  $M_s = 0.0113 \mu_B$ ,  $M_l = -0.0012 \mu_B$ . For the apical  $\text{O}_2$  ions the magnetic moments are relatively larger and equal to  $M_s = 0.118 \mu_B$ ,  $M_l = 0.0089 \mu_B$ .

#### IV. MODELLING OF PES, XAS, and XMCD SPECTRA

We will continue with the analysis of valence band states, which can be experimentally probed by photoemission and X-ray emission spectroscopy. Figure 6(a)

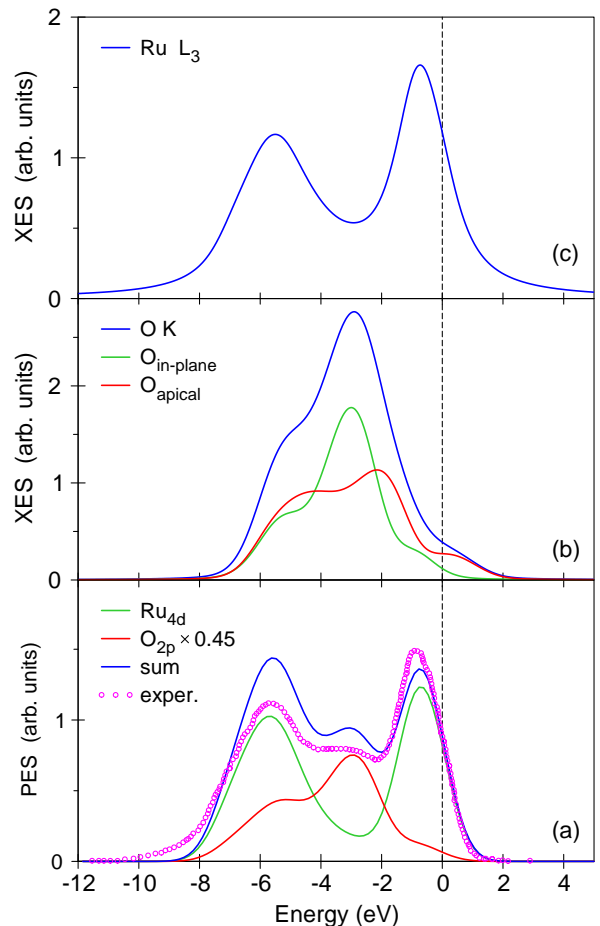


FIG. 6: (Color online) (a) The experimental valence-band photoemission spectrum of  $\text{Ca}_2\text{RuO}_4$  (magenta circles) [74] obtained at room temperature compared with the theoretically calculated Ru 4d (full green curve) and O 2p (multiplied by the factor 0.45, full green curve) partial DOSs in the GGA+SO+ $U$  approximation. (b) and (c) Calculated XES spectra for O  $K$ - and Ru  $L_3$ - edges, respectively.

presents the experimentally obtained valence-band photoemission spectrum of  $\text{Ca}_2\text{RuO}_4$  (magenta circles) [74], compared with the theoretically calculated partial DOSs for Ru 4d and O 2p computed within the GGA+SO+ $U$  approximation. The closest to the Fermi energy peak at  $\sim -1$  eV is derived mostly from the Ru  $t_{2g}$  states. The peak at  $-6$  eV is due to the Ru  $4d_{\text{O}}$  states with some contribution from the O 2p states. The fine structure at  $-3$  eV is completely from the O 2p states. It is known [64] that the cross section for the 4d states is larger than for the O 2p states in the valence-band PE spectra, therefore, to achieve the best agreement with the experimental PES spectrum one has to reduce the contribution from the O 2p partial DOS in comparison with the Ru 4d states.

Figures 6(b) and 6(c) present the theoretically calculated XES spectra for the oxygen  $K$  and Ru  $L_3$  edges, respectively. The Ru  $L_3$  XES spectrum has a two peak structure. These peaks reflect the energy position of the

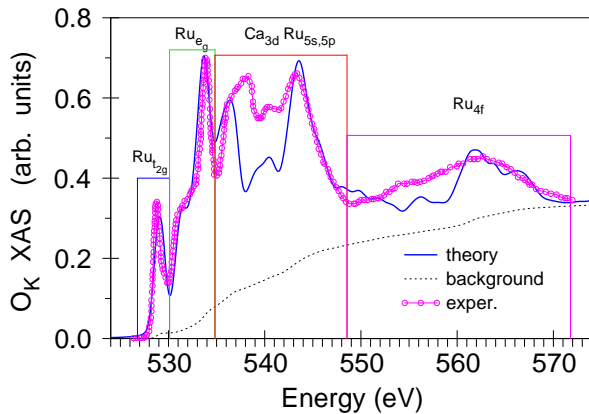


FIG. 7: (Color online) The experimental O  $K$ -edge XAS spectrum of  $\text{Ca}_2\text{RuO}_4$  taken at 90 K in TEY mode [74], shown in comparison with the theoretical spectrum calculated within the GGA+SO+ $U$  approximation using  $U_{\text{eff}} = 0.5$  eV.

Ru  $t_{2g}$  and  $4d_{\text{O}}$  states similar to the corresponding peaks in the PES spectrum. The width of the O  $K$  XES spectrum is much smaller than the Ru  $L_3$  XES spectrum and the spectrum consists of a major peak at  $-3$  eV with a low energy shoulder at  $\sim -5$  eV. The shapes of the XES individual spectra from the planar (the green curve) and apical (the red curve) oxygen are quite different. Experimental measurements of the XES at the Ru  $L_3$  and oxygen  $K$  edges are highly desirable.

X-ray absorption spectra reflect the energy distribution of empty states in crystals. Figure 7 presents the experimentally measured oxygen  $K$  XAS spectrum of  $\text{Ca}_2\text{RuO}_4$  [74] in comparison with the theoretically calculated spectrum in the GGA+SO+ $U$  approximation in a wide energy interval. The spectrum can be subdivided in several parts. The low energy peak at 528.8 eV is due to dipole transitions from the  $1s$  core state into the empty oxygen  $2p$  states derived from the hybridization with the Ru UHB  $t_{2g}$  peak situated just above the Fermi level (see Fig. 5). The next peak at 534 eV with a low energy shoulder at 531 eV is due to transitions into the oxygen  $2p$  empty states derived from the hybridization with Ru  $e_g$  states. The fine structures located between 535 and 549 eV reflect the energy distribution of the  $\text{Ca}_{3d}$  and  $\text{Ru}_{5s,5p}$  states. The wide high energy peak at 549-573 eV is due to dipole transitions from the  $1s$  core state into the empty oxygen  $2p$  states derived from the hybridization with the  $\text{Ru}_{4f}$  and free electron-like states. Although the experimental O  $K$  XAS spectrum spreads over a very wide energy interval ( $\sim 45$  eV), the theory quite well describes all peculiarities of the experimental spectrum, however, it slightly underestimates the intensity at 536-543 eV.

Figure 8 (the upper panel) shows the experimental XAS spectrum at the Ru  $L_3$  edge of  $\text{Ca}_2\text{RuO}_4$  [45] in comparison with the theoretically calculated one. The lower panel shows the theoretically calculated Ru  $L_{2,3}$

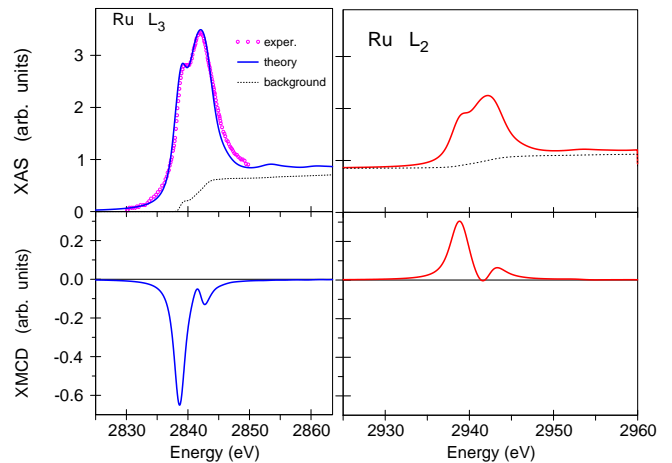


FIG. 8: (Color online) **Upper panel.** The experimental Ru  $L_3$ -edge XAS spectrum of  $\text{Ca}_2\text{RuO}_4$  (magenta circles) taken at room temperature [45], shown in comparison with the theoretical spectrum calculated within the GGA+SO+ $U$  approximation (the solid blue curve). The dotted black curve represents the background scattering intensity. The theoretical Ru  $L_2$ -edge XAS spectrum is also shown in red. **Lower panel.** Theoretically calculated Ru  $L_{2,3}$  XMCD spectra.

XMCD spectra. Two features can be observed in the experimental Ru  $L_3$  XAS spectrum at incident energies of  $E_1 = 2838.5$  eV and  $E_2 = 2841$  eV, corresponding to  $2p_{3/2} \rightarrow 4d_{t_{2g}}$  and  $2p_{3/2} \rightarrow 4d_{e_g}$  transitions, respectively [45]. The isotropic  $L_{2,3}$  XAS spectra are dominated by the empty  $e_g$  states with a smaller contribution from the empty  $t_{2g}$  orbitals at lower energy. The XMCD spectra, however, mainly come from the  $t_{2g}$  orbitals ( $J_{\text{eff}} = 1/2$ ). This results in a shift between the maxima of the XAS and XMCD spectra.

Due to the importance of SOC effects in ruthenates and iridates, it is natural to quantify the strength of the SO interactions in these compounds. One method of accomplishing this is provided by the XAS spectroscopy. Van der Laan and Thole showed that the so-called branching ratio  $\text{BR} = I_{L_3}/I_{L_2}$  ( $I_{L_{2,3}}$  is the integrated intensity of the isotropic XAS at the  $L_{2,3}$  edges) is an important quantity in the study of  $4d$  and  $5d$  oxides related to the SO interaction [75]. The BR is directly related to the ground-state expectation value of the angular part of the spin-orbit coupling  $\langle \mathbf{L} \cdot \mathbf{S} \rangle$  through  $\text{BR} = (2+r)/(1-r)$ , with  $r = \langle \mathbf{L} \cdot \mathbf{S} \rangle / n_h$  and  $n_h$  is the number of holes in  $d$  states [75]. As a result, XAS provides a direct probe of SO interactions, which is complementary to other techniques such as the magnetic susceptibility, electron paramagnetic resonance, and Mössbauer spectroscopy (which probe SOC through the value of the Lande  $g$ -factor). In the limit of negligible SOC effects the statistical branching ratio  $\text{BR} = 2$ , and the  $L_3$  white line is twice the size of the  $L_2$  feature [75]. A strong deviation from 2 indicates a strong coupling between the local orbital and spin moments. Our DFT calculations

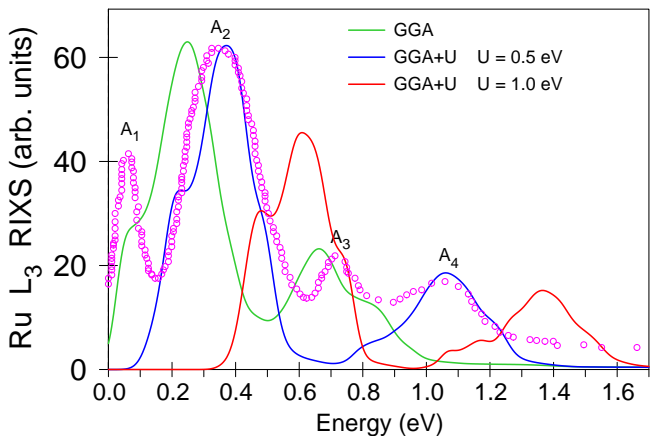


FIG. 9: (Color online) The experimental RIXS spectrum of  $\text{Ca}_2\text{RuO}_4$  at the Ru  $L_3$  edge, obtained by Bertinshaw *et al.* [54] (open magenta circles), for the  $t_{2g} \rightarrow t_{2g}$  transitions, shown in comparison with theoretical RIXS spectra calculated using different approximations.

produce  $\text{BR} = 2.46$  for the GGA+SO+ $U$  ( $U_{\text{eff}} = 0.5$  eV) approximation. We should mention that, although, the BR ratio in  $\text{Ca}_2\text{RuO}_4$  is larger than the statistical ratio in the absence of orbital magnetization, it is still smaller in comparison with iridates with strong SOC, such as  $\text{Sr}_2\text{IrO}_4$ , where the measured BR is close to 4.1 [76] and the theoretically calculated one is equal to 3.56 [72]. It indicates that SOC is less important in  $\text{Ca}_2\text{RuO}_4$  in comparison with iridates.

## V. RIXS SPECTRA

### A. Ru $L_3$ RIXS spectrum

The RIXS spectra at the Ru  $L_{2,3}$  edges arise from local excitations between the filled and empty  $4d$  states. More precisely, the incoming photon excites a  $2p_{1/2}$  core electron ( $L_2$  spectrum) or a  $2p_{3/2}$  one ( $L_3$  spectrum) into an empty  $4d$  state, which is subsequently followed by a de-excitation from an occupied  $4d$  state into the core level. Because of the dipole selection rules, apart from  $5s_{1/2}$ -states (which have a small contribution to RIXS due to relatively small  $2p \rightarrow 5s$  matrix elements [64]) only  $4d_{3/2}$ -states occur for  $L_2$  RIXS, whereas for  $L_3$  RIXS  $4d_{5/2}$ -states also contribute. Although the  $2p_{3/2} \rightarrow 4d_{3/2}$  radial matrix elements are only slightly smaller than the  $2p_{3/2} \rightarrow 4d_{5/2}$  ones, the angular matrix elements strongly suppress the  $2p_{3/2} \rightarrow 4d_{3/2}$  contribution [64]. Therefore, the RIXS spectrum at the Ru  $L_3$  edge can be viewed as interband transitions between  $4d_{5/2}$  states.

Ru  $t_{2g}$  LEB and UEB states have two and one DOS peaks, respectively (see Figs. 4 and 5). The interband transitions between these peaks produce a two peak structure in the intra- $t_{2g}$  excitations. The energy po-

sition of these two peaks are very sensitive to the relative position of the  $t_{2g}$  LEB and UEB. Figure 9 shows the experimental RIXS spectrum obtained by Bertinshaw *et al.* [54] (open magenta circles) compared with the theoretical spectra calculated for the  $t_{2g} \rightarrow t_{2g}$  transitions in different theoretical approaches. The GGA+SO approximation produces the RIXS spectrum in pure agreement with the experimental data. The best agreement was found for the GGA+SO+ $U$  approximation with  $U_{\text{eff}} = 0.5$  eV. The calculations with larger values of  $U_{\text{eff}}$  shift the RIXS spectra towards higher energies. The experiment produces four peaks  $A_1$ ,  $A_2$ ,  $A_3$ , and  $A_4$  at 0.05, 0.32, 0.75, and 1.0 eV (Fig. 9) below 1.5 eV. Our calculations show a two peak structure for the  $t_{2g} \rightarrow t_{2g}$  transitions. There are no peaks  $A_1$  and  $A_3$  in the DFT calculations. The lowest peak  $A_1$  at 0.05 eV was interpreted as magnetic excitations [45] in consistency with neutron and Raman scattering measurements [43, 44].

Gretarsson *et al.* [45] obtained the photon polarization dependence of the RIXS intensity, which was modulated by angle  $\theta$  between the incoming beam and the  $\text{RuO}_2$  planes of  $\text{Ca}_2\text{RuO}_4$ . When increasing  $\theta$ , the polarization of the incoming photon moves from the sample  $c$  axis into the  $ab$  plane. The authors used a fixed angle of  $90^\circ$  between incoming and outgoing photon beams. Such investigation can provide additional clues to the origin of the different features of the RIXS spectrum. The authors found very strong dependence of intensity of the  $A_2$  and  $A_4$  features as a function of angle  $\theta$ . On the other hand, such dependence was extremely weak for the  $A_3$  peak. It can indicate that peak  $A_3$  (which is absent in our DFT calculations) possesses quite different nature in comparison with peaks  $A_2$  and  $A_4$ . Besides, the experimental O  $K$ -edge RIXS spectra of  $\text{Ca}_2\text{RuO}_4$  exhibit only two peaks below 1.5 eV [77]. It is natural to suggest that peak  $A_3$  might have excitonic nature. It is interesting to note that the reference iridate  $\text{Sr}_2\text{IrO}_4$  also possesses four experimental peaks for the  $t_{2g} \rightarrow t_{2g}$  transitions [78] and only two peaks appear in the DFT calculations [72]. The low energy peak at 0.1 eV was considered in Ref. [78] as magnon excitations in agreement with scanning tunneling microscope measurements [79]. Peak at 0.5 eV, which was absent in the DFT calculations, was attributed to an excitonic excitation in Refs. [78, 80]. The theoretical description of magnon and exciton spectra demands a many-body approach beyond the one-particle approximation, such as the Bethe-Salpiter equation for exciton spectra and calculations of the magnon dispersion and the electron-magnon interaction for magnon spectra.

The Ru  $L_3$  edge RIXS spectrum of  $\text{Ca}_2\text{RuO}_4$  reveals several peaks above the intra- $t_{2g}$  excitations at higher energies (Fig. 10). Peak  $B$  located between 2.5 eV and 4 eV is mostly due to  $t_{2g} \rightarrow e_g$  transitions (the green curve) with some additional  $\text{O}_{2p} \rightarrow t_{2g}$  and  $\text{O}_{2p} \rightarrow e_g$  (black dashed and blue dotted curves, respectively) transitions. Fine structure  $C$  at 5 to 7 eV (the red curve) is due to  $4d_{\text{O}} \rightarrow t_{2g}$  transitions. The theoretical calculations are in good agreement with the experimental data.

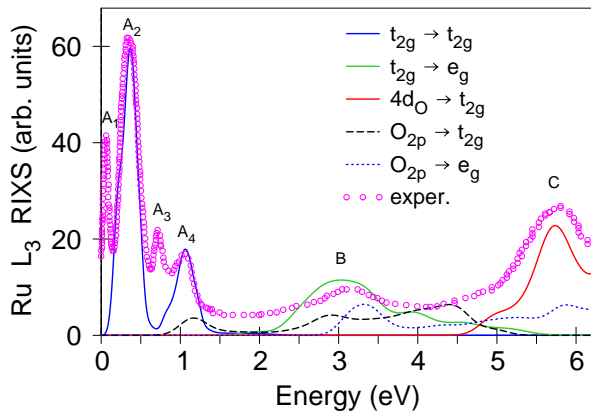


FIG. 10: (Color online) The experimental RIXS spectrum measured by Bertinshaw *et al.* [54] (open magenta circles) at the Ru  $L_3$  edge of  $\text{Ca}_2\text{RuO}_4$  for  $\theta = 45^\circ$  compared with the theoretically calculated partial contributions from different interband transitions in the GGA+SO+ $U$  ( $U_{\text{eff}} = 0.5$  eV) approximation.

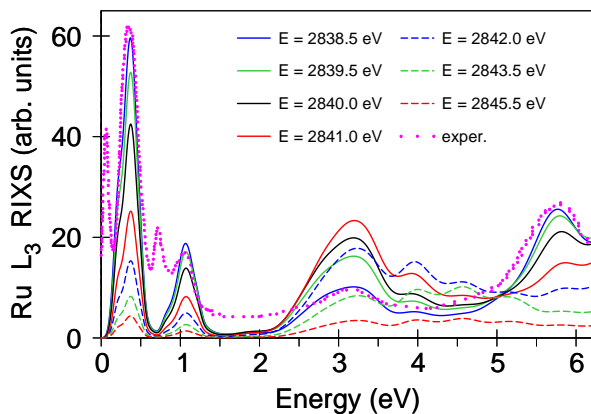


FIG. 11: (Color online) The Ru  $L_3$  RIXS spectra obtained as a function of incident photon energy  $E_i$  calculated at the Ru  $L_3$  edge in  $\text{Ca}_2\text{RuO}_4$  with the momentum transfer vector  $\mathbf{Q} = (0, 0, 3.75)$  in reciprocal lattice units in comparison with the experimental RIXS spectrum measured for  $\theta = 45^\circ$  [54].

Figure 11 shows the Ru  $L_3$  RIXS spectra obtained as a function of incident photon energy  $E_i$  calculated in  $\text{Ca}_2\text{RuO}_4$  for  $\theta = 45^\circ$  with the momentum transfer vector  $\mathbf{Q} = (0, 0, 3.75)$  in reciprocal lattice units in comparison with the experimental RIXS spectrum measured for  $\theta = 45^\circ$  [54]. Peak  $A_2$  is monotonically decreased with increasing the incident photon energy from  $E_1 = 2838.5$  eV which corresponds to the  $4d_{t_{2g}}$  edge. On the other hand, the intensity of peak  $B$  at 2.5-4 eV which is derived from the  $2p_{3/2} \rightarrow 4d_{e_g}$  transitions is increased from  $E_1$  to  $E_2 = 2841$  eV (which corresponds to the  $4d_{e_g}$  edge) and then decreased with the further increase of energy.

It is widely believed that  $d-d$  excitations show only small momentum transfer vector  $\mathbf{Q}$  dependence in  $d$  tran-

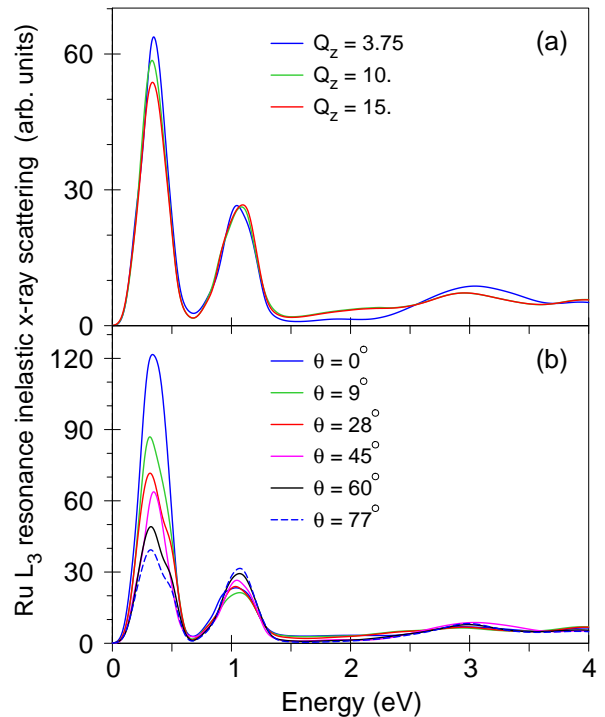


FIG. 12: (Color online) (a) The RIXS spectra at the Ru  $L_3$  edge in  $\text{Ca}_2\text{RuO}_4$  calculated as a function of  $Q_z$  with the momentum transfer vector  $\mathbf{Q} = (0, 0, Q_z)$  in reciprocal lattice units for incident photon energy  $\hbar\omega_{in} = 2838.5$  eV ( $\theta = 45^\circ$ ); (b) the RIXS spectra at the Ru  $L_3$  edge of  $\text{Ca}_2\text{RuO}_4$  calculated as a function of  $\theta$ .

sition metal compounds [81, 82]. In particular,  $\text{Ca}_2\text{RuO}_4$  has a layered-perovskite structure, therefore, the momentum dependence along the  $c$  axis is expected to be small, as in high- $T_c$  cuprates [83]. Indeed, as we see in the upper panel of Fig. 12, the RIXS spectra are almost identical for the transfer vectors  $\mathbf{Q} = (0, 0, 3.75)$ ,  $(0, 0, 10)$ , and  $(0, 0, 20)$ . Similar dependence was experimentally observed also in quasi-two dimensional  $\text{Sr}_2\text{IrO}_4$  by Ishii *et al.* [84].

Figure 12(b) shows the RIXS spectra at the Ru  $L_3$  edge for  $\text{Ca}_2\text{RuO}_4$ , calculated as a function of the angle  $\theta$ , and reveals their very strong polarization dependence. The intensity of peak  $A_2$  at 0.32 eV is strongly decreased with decreasing  $\theta$  from  $0^\circ$  to  $90^\circ$ . Very similar dependence was observed experimentally by Gretarsson *et al.* [45].

## B. Oxygen $K$ RIXS spectrum

Figure 13 shows the theoretically calculated partial contributions to the O  $K$  RIXS spectrum for  $\text{Ca}_2\text{RuO}_4$  from different interband transitions for  $\theta = 40^\circ$  (the upper panel) and  $\theta = 80^\circ$  (the lower panel) in comparison with the experimental data presented by Das *et al.* [77].

The O  $K$  RIXS spectrum consists of three major inelastic excitations: a double peak at  $\leq 1.5$  eV (blue

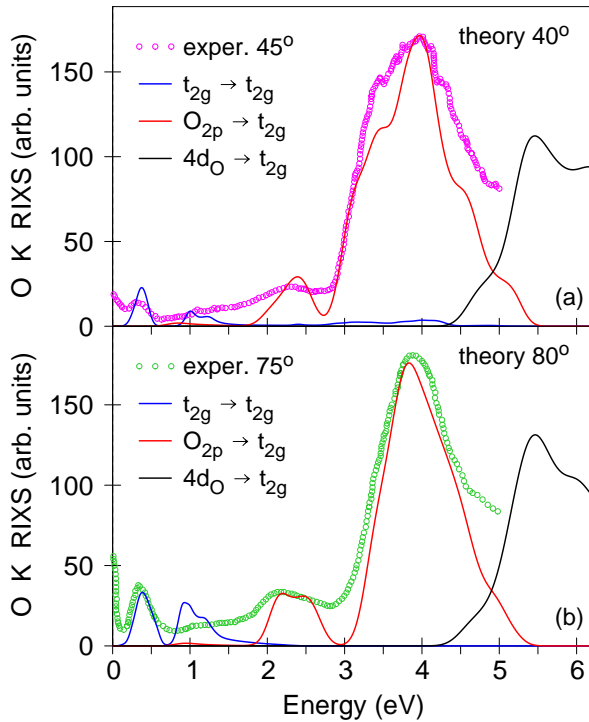


FIG. 13: (Color online) The experimentally measured O  $K$  RIXS spectrum in  $\text{Ca}_2\text{RuO}_4$  [77] (open magenta circles) in comparison with the theoretically calculated partial contributions from different interband transitions calculated in the GGA+SO+ $U$  approximation with  $U_{\text{eff}} = 0.5$  eV.

curves), a major peak between 2 and 5 eV with a low energy shoulder at 2-3 eV (red curves), and a less intensive structure at 4.5-7 eV (black curves). We found that the first double peak low energy feature is due to the interband transitions between the occupied and empty O  $2p$  states that appear as a result of the strong hybridization between oxygen  $2p$  states with Ru  $t_{2g}$  LEB and UEB in the close vicinity of the Fermi level (see Fig. 5), therefore, the oxygen  $K$  RIXS spectroscopy can be used for the estimation of the positions of Ru  $4d$  Hubbard bands. The major peak between 2 and 5 eV reflects the interband transitions between the occupied O  $2p$  states and the empty oxygen states that originate from the hybridization with Ru  $t_{2g}$  states. The fine structure between 4.5 and 7.8 eV is due to the  $4d_{\text{O}} \rightarrow t_{2g}$  interband transitions.

The polarization dependence of the RIXS spectrum for the oxygen  $K$  edge presented in Fig. 13 is much weaker compared to the corresponding dependence for the Ru  $L_3$  edge. Upon changing from  $\theta = 40^\circ$  to  $\theta = 80^\circ$  the two low energy peaks of the O  $K$  RIXS spectrum below 1.5 eV are slightly increased in intensity and the major peak between 3 and 5 eV becomes more narrow losing some fine structures.

Figure 14 shows the O  $K$  RIXS spectra as a function of incident photon energy calculated in  $\text{Ca}_2\text{RuO}_4$  for  $\theta = 80^\circ$ . With increasing the incident photon energy from  $E_i$

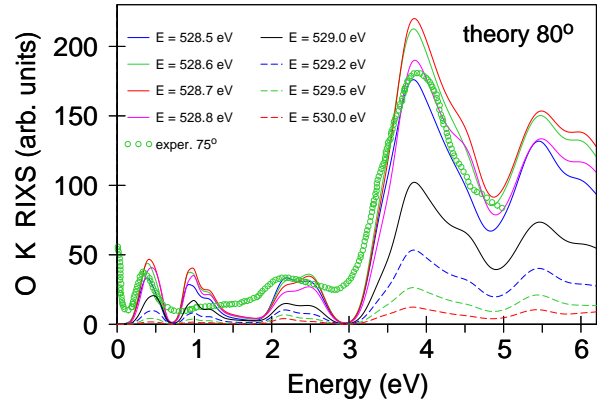


FIG. 14: (Color online) The RIXS spectra as a function of incident photon energy calculated at the O  $K$  edge in  $\text{Ca}_2\text{RuO}_4$  for  $\theta = 80^\circ$  in comparison with the experimental measurements for  $\theta = 75^\circ$  [77].

$= 528.5$  eV, the peaks increase and then after  $E_i = 528.7$  eV rapidly decrease and almost vanish for  $E_i \geq 530$  eV.

## VI. KEY FINDINGS and CONCLUSIONS

To summarize, we have thoroughly investigated the electronic and magnetic properties of the single-layered perovskite  $\text{Ca}_2\text{RuO}_4$  system theoretically, within the fully relativistic spin-polarized Dirac approach. We have performed theoretical modeling of the XES, PES, XAS, XMCD, and RIXS spectra at the Ru  $L_{2,3}$  and O  $K$  edges, comparing our results with available literature data. Our findings indicate that the intricate interplay of electron correlations, SOC, intersite hoppings, Hund's coupling, as well as the CEF gives rise to a strongly competing ground state in  $\text{Ca}_2\text{RuO}_4$ . It is widely accepted that  $\text{Ca}_2\text{RuO}_4$  is a Mott insulator, as it remains insulating above the Néel temperature and exhibits Curie-Weiss magnetic susceptibility [46]. The results of detailed ARPES measurements on  $\text{Ca}_2\text{RuO}_4$  [47] further support the presence of an orbitally differentiated band-Mott insulating ground state.  $\text{Ca}_2\text{RuO}_4$  is reported to undergo a series of phase transitions upon cooling: a metal-to-insulator transition beginning at 357 K, followed by orbital ordering at 260 K, and further by AFM ordering at 110 K. Our band structure calculations reveal that the canted noncollinear AFM ordering  $\text{AFM}_{010}^{\text{NC}}$ , characterized by an energy gap between the fully occupied  $J_{\text{eff}} = 3/2$  and empty  $J_{\text{eff}} = 1/2$  states, is energetically favored compared to nonmagnetic, ferromagnetic, or other AFM configurations. This finding highlights the critical role of SOC and electronic correlations in stabilizing the ground state of  $\text{Ca}_2\text{RuO}_4$ .

SOC splits the  $t_{2g}$  manifold into a lower  $J_{\text{eff}} = 3/2$  quartet and an upper  $J_{\text{eff}} = 1/2$  doublet in  $\text{Ca}_2\text{RuO}_4$ . The functions of the  $J_{\text{eff}} = 3/2$  quartet are dominated by  $d_{3/2}$  states with some weight of  $d_{5/2}$  ones, the  $J_{\text{eff}}$

$= 1/2$  functions are almost completely given by linear combinations of  $d_{5/2}$  states. From our GGA+SO+ $U$  calculations, we obtained the ratio  $I_{L_3}/I_{L_2}$ , known also as the BR ratio, and employed as a direct probe of the magnitude of SOC, which is found to be 2.46 for  $\text{Ca}_2\text{RuO}_4$ . Although this value exceeds the statistical ratio in the absence of orbital magnetization, it remains significantly smaller than that observed for the case of iridates with particularly strong SOC, such as  $\text{Sr}_2\text{IrO}_4$ , where the measured BR approaches a value of 4.1 [76]. This implies that SOC effects are essentially weaker in  $\text{Ca}_2\text{RuO}_4$  than in these iridate compounds.

The energy gap in  $\text{Ca}_2\text{RuO}_4$  opens up only when Hubbard electron-electron correlations are taken into account. However, the effective Hubbard parameter  $U_{\text{eff}}^c$  strongly depends on magnetic ordering. Consequently,  $\text{Ca}_2\text{RuO}_4$  exhibits a mixed Slater and Mott character.

We have thoroughly investigated the nature of the RIXS spectra at the Ru  $L_3$  and O  $K$  edges through theoretical modeling. The best agreement between the calculated and experimentally obtained RIXS spectra was achieved within the GGA+SO+ $U$  approximation using the effective Hubbard parameter  $U_{\text{eff}} = 0.5$  eV.

Ru  $t_{2g}$  LEB and UEB states have two and one DOS peaks, respectively. The interband transitions between these peaks produce a two major peak structure in the intra- $t_{2g}$  excitations. However, the experiment produces four peaks  $A_1$ ,  $A_2$ ,  $A_3$ , and  $A_4$  at 0.05, 0.32, 0.75, and 1.0 eV below 1.5 eV. The lowest peak  $A_1$  at 0.05 eV can be interpreted as magnetic excitations [45] in consistency with neutron and Raman scattering measurements [43, 44]. There is very strong photon polarization dependence of the  $A_2$  and  $A_4$  features. On the other hand, such dependence was extremely weak for peak  $A_3$ . This may indicate that peak  $A_3$ , which does not appear in our DFT calculations, has a fundamentally different origin compared to peaks  $A_2$  and  $A_4$ . We propose that peak  $A_3$  may be of excitonic nature. A theoretical treatment of magnon and excitonic excitations requires a more advanced approach beyond the one-particle approximation.

The Ru  $L_3$  edge RIXS spectrum of  $\text{Ca}_2\text{RuO}_4$  reveals several peaks above the intra- $t_{2g}$  excitations at higher energies. Peak  $B$  located between 2.5 eV and 4 eV is mostly due to  $t_{2g} \rightarrow e_g$  transitions with some additional  $\text{O}_{2p} \rightarrow t_{2g}$  and  $\text{O}_{2p} \rightarrow e_g$  transitions. Fine structure  $C$  at 5 to 7 eV is due to the  $4d_{\text{O}} \rightarrow t_{2g}$  transitions. The theoretical calculations are in good agreement with the experimental data.

We found very strong polarization dependence of the RIXS spectrum at the Ru  $L_3$  edge. The intensity of peak  $A_2$  at 0.32 eV is strongly decreased upon decreasing angle  $\theta$  from  $0^\circ$  to  $90^\circ$ . On the other hand, due to the quasi-two dimensional crystal structure of  $\text{Ca}_2\text{RuO}_4$ , the momentum dependence of the RIXS spectrum along the  $c$  axis was found to be very small.

The investigation of the Ru  $L_3$  RIXS spectra as a function of incident photon energy  $E_i$  shows that peak  $A_2$  is monotonically decreased with increasing the incident photon energy from  $E_1 = 2838.5$  eV, which corresponds to the  $4d_{t_{2g}}$  edge. On the other hand, the intensity of peak  $B$  at 2.5-4 eV, which is derived from the  $2p_{3/2} \rightarrow 4d_{e_g}$  transitions, increases from  $E_1$  to  $E_2 = 2841$  eV (which corresponds to the  $4d_{e_g}$  edge) and then decreases with the further increase of energy.

The O  $K$  RIXS spectrum consists of three major inelastic excitations: a double peak at  $\leq 1.5$  eV, a major peak between 2 and 5 eV with a low energy shoulder at 2-3 eV, and a less intensive structure at 4.5-7 eV. We found that the first double peak at low energy is due to the interband transitions between the occupied and empty  $2p$  oxygen states that appear as a result of the strong hybridization between oxygen  $2p$  states with Ru  $t_{2g}$  LEB and UEB in the close vicinity of the Fermi level. The next major peak between 2 and 5 eV reflects the interband transitions from the occupied O  $2p$  states and the empty oxygen states that originate from the hybridization with Ru  $t_{2g}$  states. The fine structure between 4.5 and 7.8 eV is due to the  $4d_{\text{O}} \rightarrow t_{2g}$  interband transitions. The polarization dependence of the RIXS spectrum for the oxygen  $K$  edge is much weaker in comparison with the corresponding dependence for the Ru  $L_3$  edge. Upon changing from  $\theta = 40^\circ$  to  $\theta = 80^\circ$  the low energy RIXS peaks below 1.5 eV are slightly increased in intensity and the major RIXS peak between 3 and 5 eV becomes more narrow losing some fine structures.

We found much stronger dependence on the incident photon energy in the case of the O  $K$  RIXS spectrum in comparison with the corresponding dependence at the Ru  $L_3$  edge. With increasing the incident photon energy from  $E_i = 528.5$  eV, the peaks increase and then after  $E_i = 528.7$  eV rapidly decrease and almost vanish for  $E_i \geq 530$  eV.

## Acknowledgments

We are thankful to Dr. Alexander Yaresko from the Max Planck Institute FKF in Stuttgart for helpful discussions. This work was supported by the Ministry of Education and Science of Ukraine within the Ukrainian-Austrian Joint Programme of Scientific and Technological Cooperation, project "Resonant inelastic x-ray scattering in complex 5d oxides from first principles" (Agrmt. No. M/73-2025, Reg. No. 0125U003444). The authors P.F. Perndorfer, P.A. Buczek and A. Ernst acknowledge the funding by the Fonds zur Förderung der wissenschaftlichen Forschung (FWF) under Grant No. I 5384 / DFG-LAV grant "SPINELS" BU 4062/1-1.

- 
- [1] B. J. Kim, H. Jin, S. J. Moon, J.-Y. Kim, B.-G. Park, C. S. Leem, J. Yu, T. W. Noh, C. Kim, S.-J. Oh, et al., *Phys. Rev. Lett.* **101**, 076402 (2008).
- [2] B. J. Kim, H. Ohsumi, T. Komesu, S. Sakai, T. Morita, H. Takagi, and T. Arima, *Science* **323**, 1329 (2009).
- [3] G. Jackeli and G. Khaliullin, *Phys. Rev. Lett.* **102**, 017205 (2009).
- [4] G. Chen, R. Pereira, and L. Balents, *Phys. Rev. B* **82**, 174440 (2010).
- [5] W. Witczak-Krempa, G. Chen, Y. Kim, and L. Balents, *Annu. Rev. Condens. Matter Phys.* **5**, 57 (2014).
- [6] X.-L. Qi and S.-C. Zhang, *Physics Today* **63**, 33 (2010).
- [7] Y. Ando, *J. Phys. Soc. Jpn.* **82**, 102001 (2013).
- [8] T. O. Wehling, A. Black-Schaffer, and A. Balatsky, *Adv. Phys.* **63**, 1 (2014).
- [9] A. Bansi, L. H, and T. Das, *Rev. Mod. Phys.* **88**, 021004 (2016).
- [10] H. Watanabe, T. Shirakawa, and S. Yunoki, *Phys. Rev. Lett.* **105**, 216410 (2010).
- [11] C. Martins, M. Aichhorn, L. Vaugier, and S. Biermann, *Phys. Rev. Lett.* **107**, 266404 (2011).
- [12] W. Witczak-Krempa and Y. B. Kim, *Phys. Rev. B* **85**, 045124 (2012).
- [13] A. Go, W. Witczak-Krempa, G. S. Jeon, K. Park, and Y. B. Kim, *Phys. Rev. Lett.* **109**, 066401 (2012).
- [14] A. B. Sushkov, J. B. Hofmann, G. S. Jenkins, J. Ishikawa, S. Nakatsuji, S. DasSarma, and H. D. Drew, *Phys. Rev. B* **92**, 241108 (2015).
- [15] I. Kimchi, J. G. Analytis, and A. Vishwanath, *Phys. Rev. B* **90**, 205126 (2014).
- [16] L. S. I. Veiga, M. Etter, K. Glazyrin, F. Sun, J. C. A. Escanhoela, G. Fabbri, J. R. L. Mardegan, P. S. Malavi, Y. Deng, P. P. Stavropoulos, et al., *Phys. Rev. B* **96**, 140402(R) (2017).
- [17] V. Hermann, M. Altmeyer, J. Ebad-Allah, F. Freund, A. Jesche, A. A. Tsirlin, M. Hanfland, P. Gegenwart, I. I. Mazin, D. I. Khomskii, et al., *Phys. Rev. B* **97**, 020104(R) (2018).
- [18] V. N. Antonov, L. V. Bekenov, and D. A. Kukusta, *Phys. Rev. B* **102**, 195134 (2020).
- [19] V. N. Antonov, D. A. Kukusta, L. Uba, A. Bonda, and S. Uba, *Phys. Rev. B* **103**, 235127 (2021).
- [20] V. N. Antonov, S. Uba, and L. Uba, *Phys. Rev. B* **98**, 245113 (2018).
- [21] T. Dodds, T.-P. Choy, and Y. B. Kim, *Phys. Rev. B* **84**, 104439 (2011).
- [22] G. Chen and L. Balents, *Phys. Rev. B* **84**, 094420 (2011).
- [23] O. N. Meetei, O. Erten, M. Randeria, N. Trivedi, and P. Woodward, *Phys. Rev. Lett.* **110**, 087203 (2013).
- [24] C. Svoboda, W. Zhang, M. Randeria, and N. Trivedi, *Phys. Rev. B* **104**, 024437 (2021).
- [25] Q. Chen, C. Svoboda, Q. Zheng, B. C. Sales, D. G. Mandrus, H. D. Zhou, J.-S. Zhou, D. McComb, M. Randeria, N. Trivedi, et al., *Phys. Rev. B* **96**, 144423 (2017).
- [26] A. Earnshaw, B. Figgis, J. Lewis, and R. Peacock, *J. Chem. Soc. (Resumed)* **0**, 3132 (1961).
- [27] G. Cao, T. F. Qi, L. Li, J. Terzic, S. J. Yuan, L. E. DeLong, G. Murthy, and R. K. Kaul, *Phys. Rev. Lett.* **112**, 056402 (2014).
- [28] G. Khaliullin, *Phys. Rev. Lett.* **111**, 197201 (2013).
- [29] Y. Maeno, H. Hashimoto, K. Yoshida, S. Nishizaki, T. Fujita, J. G. Bednorz, and F. Lichtenberg, *Nature (London)* **372**, 532 (1994).
- [30] Y. Maeno, T. M. Rice, and M. Sigrist, *Phys. Today* **54**, 42 (2001).
- [31] G. Cao, S. McCall, M. Shepard, J. E. Crow, and R. P. Guertin, *Phys. Rev. B* **56**, 321 (1997).
- [32] L. Klein, L. Antognazza, T. H. Geballe, M. R. Beasley, and A. Kapitulnik, *Phys. Rev. B* **60**, 1448 (1999).
- [33] C. Sow, S. Yonezawa, S. Kitamura, T. Oka, K. Kuroki, F. Nakamura, and Y. Maeno, *Science* **358**, 1084 (2017).
- [34] H. Nobukane, K. Yanagihara, Y. Kunisada, Y. Ogasawara, K. Nomura, Y. Asano, and j. y. S. Tanda, title=Observation of Localized High-T<sub>c</sub> Superconductivity in a Ca<sub>2</sub>RuO<sub>4</sub> Nanofilm Single Crystal (????).
- [35] P. L. Alireza, F. Nakamura, S. K. Goh, Y. Maeno, S. Nakatsuji, Y. T. C. K. aand M. Sutherland, S. Julian, and G. G. Lonzarich, *J. Phys.: Condens. Matter* **22**, 052202 (2010).
- [36] M. Braden, G. Andre, S. Nakatsuji, and Y. Maeno, *Phys. Rev. B* **58**, 847 (1998).
- [37] C. S. Alexander, G. Cao, V. Dobrosavljevic, S. McCall, J. E. Crow, E. Lochner, and R. P. Guertin, *Phys. Rev. B* **60**, R8422 (1999).
- [38] O. Friedt, M. Braden, G. Andr e, P. Adelman, S. Nakatsuji, and Y. Maeno, *Phys. Rev. B* **63**, 174432 (2001).
- [39] P. Steffens, O. Friedt, P. Alireza, W. G. Marshall, W. Schmidt, F. Nakamura, S. Nakatsuji, Y. Maeno, R. Lengsdorf, M. M. AbdElmeguid, et al., *Phys. Rev. B* **72**, 094104 (2005).
- [40] I. Zegkinoglou, J. Stremper, C. S. Nelson, J. P. Hill, J. Chakhalian, C. Bernhard, J. C. Lang, G. Srajer, H. Fukazawa, S. Nakatsuji, et al., *Phys. Rev. Lett.* **95**, 136401 (2005).
- [41] D. G. Porter, V. Granata, F. Forte, S. D. Matteo, M. Cuoco, R. Fittipaldi, A. Vecchione, and A. Bombardi, *Phys. Rev. B* **98**, 125142 (2018).
- [42] K. I. Kugel, D. I. Khomskii, A. O. Sboychakov, and S. V. Streltsov, *Phys. Rev. B* **91**, 155125 (2015).
- [43] A. Jain, M. Krautloher, J. Porras, G. H. Ryu, D. P. Chen, D. L. Abernathy, J. T. Park, A. Ivanov, J. Chaloupka, and G. Khaliullin, *Higgs mode and its decay in a two-dimensional antiferromagnet* (2017).
- [44] S.-M. Souliou, J. Chaloupka, G. Khaliullin, G. Ryu, A. Jain, B. J. Kim, M. L. Tacon, and B. Keimer, *Phys. Rev. Lett.* **119**, 067201 (2017).
- [45] H. Gretarsson, H. Suzuki, H. Kim, K. Ueda, M. Krautloher, B. J. Kim, H. Yavas, G. Khaliullin, and B. Keimer, *Phys. Rev. B* **100**, 045123 (2019).
- [46] S. Nakatsuji, S. Ikeda, and Y. Maeno, *J. Phys. Soc. Jpn.* **66**, 1868 (1997).
- [47] D. Sutter, C. G. Fatuzzo, S. Moser, M. Kim, R. Fittipaldi, A. Vecchione, V. Granata, Y. Sassa, F. Cossalter, G. Gatti, et al., *Nat. Commun.* **8**, 15176 (2017).
- [48] E. Gorelov, M. Karolak, T. O. Wehling, F. Lechermann, A. I. Lichtenstein, and E. Pavarini, *Phys. Rev. Lett.* **104**, 226401 (2010).
- [49] C.-C. Kao, W. A. L. Caliebe, J. B. Hastings, and J.-M. Gillet, *Phys. Rev. B* **54**, 16361 (1996).
- [50] L. J. P. Ament, M. van Veenendaal, T. P. Devereaux, J. P. Hill, and J. van den Brink, *Rev. Mod. Phys.* **83**, 705 (2011).

- [51] F. M. F. de Groot, M. W. Haverkort, H. Elnaggar, A. Juhin, K.-J. Zhou, and P. Glatzel, *Nat. Rev. Methods Primers* **4**, 46 (2024).
- [52] H. Kim, G. Khaliullin, and B. J. Kim, *Phys. Rev. B* **106**, 245127 (2022).
- [53] B. J. Kim and G. Khaliullin, *Phys. Rev. B* **96**, 085108 (2017).
- [54] J. Bertinshaw, M. Krautloher, H. Suzuki, H. Takahashi, A. Ivanov, H. Yava, B. J. Kim, H. Gretarsson, and B. Keimer, *Phys. Rev. B* **103**, 085108 (2021).
- [55] S. Yamamoto, Y. Ohta, and K. Sugimoto, *Phys. Rev. B* **106**, 045136 (2022).
- [56] V. V. Nemoshkalenko, A. E. Krasovskii, V. N. Antonov, V. N. Antonov, U. Fleck, H. Wonn, and P. Ziesche, *Phys. status solidi B* **120**, 283 (1983).
- [57] E. Arola, P. Strange, and B. L. Gyorffy, *Phys. Rev. B* **55**, 472 (1997).
- [58] G. Lehmann and M. Taut, *Phys. status solidi B* **54**, 469 (1972).
- [59] V. N. Antonov, D. A. Kukusta, and L. V. Bekenov, *Phys. Rev. B* **105**, 155144 (2022).
- [60] V. N. Antonov, O. Jepsen, A. N. Yaresko, and A. P. Shpak, *J. Appl. Phys.* **100**, 043711 (2006).
- [61] V. N. Antonov, B. N. Harmon, A. N. Yaresko, and A. P. Shpak, *Phys. Rev. B* **75**, 184422 (2007).
- [62] V. N. Antonov, A. N. Yaresko, and O. Jepsen, *Phys. Rev. B* **81**, 075209 (2010).
- [63] O. K. Andersen, *Phys. Rev. B* **12**, 3060 (1975).
- [64] V. Antonov, B. Harmon, and A. Yaresko, *Electronic Structure and Magneto-Optical Properties of Solids* (Kluwer, Dordrecht, 2004).
- [65] J. P. Perdew, K. Burke, and M. Ernzerhof, *Phys. Rev. Lett.* **77**, 3865 (1996).
- [66] P. E. Blöchl, O. Jepsen, and O. K. Andersen, *Phys. Rev. B* **49**, 16223 (1994).
- [67] A. N. Yaresko, V. N. Antonov, and P. Fulde, *Phys. Rev. B* **67**, 155103 (2003).
- [68] P. H. Dederichs, S. Blügel, R. Zeller, and H. Akai, *Phys. Rev. Lett.* **53**, 2512 (1984).
- [69] W. E. Pickett, S. C. Erwin, and E. C. Ethridge, *Phys. Rev. B* **58**, 1201 (1998).
- [70] V. N. Antonov, D. A. Kukusta, and L. V. Bekenov, *Phys. Rev. B* **105**, 155145 (2022).
- [71] J. L. Campbell and T. Parr, *At. Data Nucl. Data Tables* **77**, 1 (2001).
- [72] V. N. Antonov, D. A. Kukusta, and L. V. Bekenov, *Phys. Rev. B* **109**, 165120 (2024).
- [73] D. D. Koelling and B. N. Harmon, *J. Phys. C* **10**, 3107 (1977).
- [74] T. Mizokawa, L. H. Tjeng, G. A. Sawatzky, G. Ghiringhelli, O. Tjernberg, N. B. Brookes, H. Fukazawa, S. Nakatsuji, and Y. Maeno, *Phys. Rev. Lett.* **87**, 077202 (2001).
- [75] G. van der Laan and B. T. Thole, *Phys. Rev. Lett.* **60**, 1977 (1988).
- [76] D. Haskel, G. Fabbris, M. Zhernenkov, P. P. Kong, C. Q. Jin, G. Cao, and M. van Veenendaal, *Phys. Rev. Lett.* **109**, 027204 (2012).
- [77] L. Das, F. Forte, R. Fittipaldi, C. G. Fatuzzo, V. Granata, O. Ivashko, M. Horio, F. Schindler, M. Dantz, Y. Tseng, et al., *Phys. Rev. X* **8**, 011048 (2018).
- [78] J. Kim, M. Daghofer, A. H. Said, T. Gog, J. van den Brink, G. Khaliullin, and B. J. Kim, *Nature Comm.* **5**, 4453 (2014).
- [79] J. Nichols, N. Bray-Ali, A. Ansary, G. Cao, and K.-W. Ng, *Phys. Rev. B* **89**, 085125 (2014).
- [80] J.-K. Kim, C. Dietl, H.-W. J. Kim, S.-H. Ha, J. Kim, A. H. Said, J. Kim, and B. J. Kim, *J. Synchrotron Rad.* **30**, 643 (2023).
- [81] X. Liu, V. M. Katukuri, L. Hozoi, W.-G. Yin, M. P. M. Dean, M. H. Upton, J. Kim, D. Casa, A. Said, T. Gog, et al., *Phys. Rev. Lett.* **109**, 157401 (2012).
- [82] A. Krajewska, T. Takayama, R. Dinnebier, A. Yaresko, K. Ishii, M. Isobe, and H. Takagi, *Phys. Rev. B* **101**, 121101(R) (2020).
- [83] K. Ishii, K. Tsutsui, Y. Endoh, T. Tohyama, S. Maekawa, M. Hoesch, K. Kuzushita, M. Tsubota, T. Inami, J. Mizuki, et al., *Phys. Rev. Lett.* **94**, 207003 (2005).
- [84] K. Ishii, I. Jarrige, M. Yoshida, K. Ikeuchi, J. Mizuki, K. Ohashi, T. Takayama, J. Matsuno, and H. Takagi, *Phys. Rev. B* **83**, 115121 (2011).